

Supplemental material to accompany:

Formation of miarolitic-class, segregation-type pegmatites in the Taishanmiao batholith, China: The role of pressure fluctuations and volatile exsolution during pegmatite formation in a closed, isochoric system

Yabin Yuan^{1,2}, Lowell R. Moore², Ryan J. McAleer³, Shunda Yuan¹, Hegen Ouyang¹, Harvey E. Belkin³, Jingwen Mao¹, D. Matthew Sublett Jr.², Robert J. Bodnar

¹ MLR Key Laboratory of Metallogeny and Mineral Assessment, Institute of Mineral Resources, Chinese Academy of Geological Sciences, Beijing 100037, China

² Department of Geosciences, Virginia Tech, Blacksburg, Virginia 24061, USA

³ U.S. Geological Survey, Reston, Virginia 20192, USA

ANALYTICAL METHODS AND MODELING

In order to constrain the physical conditions and geochemical processes associated with formation of the Taishanmiao pegmatites, various methods were applied to analyze MI and FI, including microthermometry, Raman spectroscopy, and EDS and WDS analyses. In addition, the Rhyolite-MELTS algorithm was applied to reconstruct the igneous evolution of the Taishanmiao granite to test the hypothesis that Taishanmiao pegmatites crystallized from a late-stage (residual) melt, representing the remains of the melt that produced the enclosing batholith, and thus represent segregation-type pegmatites.

Microthermometric analyses

Melt and fluid inclusions from four different assemblages (A2, A5, Z1 and Z2) in two different quartz crystals were analyzed by microthermometry in the Fluids Research Laboratory at Virginia Tech. Microthermometric experiments were conducted on FI from quartz crystals A5 and Z2 with a Linkam THMSG 600 heating-freezing stage. The stage was calibrated at 0.0°C and 374.1°C using synthetic pure H₂O fluid inclusions (Sterner and Bodnar, 1984), and measured temperatures are considered to be accurate to ±0.1 degrees at 0.0°C and ±1°C at 374.1°C. Phase changes observed during microthermometric analyses were the ice-melting temperature (T_m ice); clathrate melting temperature (T_m CO₂-clathrate), and liquid-vapor homogenization temperature (T_h) (Table S2). During microthermometry, the sample was cooled and/or heated quickly during the first cycle to obtain an approximation of the temperature(s) at which phase changes occur. Then, the procedure was repeated using a slower heating rate as the temperature of the phase change was approached. Salinity of the FI

and isochores were estimated with the combined results of T_m ice, T_m CO₂-clathrate and T_h based on *PVTX* phase behavior in the H₂O-NaCl-CO₂ system (Steele-MacInnis, 2018).

Because all of the MI were partially to completely crystallized, it was first necessary to homogenize the MI before conducting Raman and electron probe microanalysis. MI were homogenized in a microscope-mounted Linkam TS1400XY heating stage (Esposito et al., 2012). During heating experiments to homogenize the MI, N₂ gas was circulated through the stage to prevent oxidation of the sample at high temperature, which causes the MI to become opaque and affects the ability to monitor the MI optically (see Esposito et al., 2012). In this study, a heating rate of 50°C/min was applied between 22°C - 600°C. Then, the heating rate was decreased to 30°C/min during continued heating. Evidence of melting was observed in some MI at ~680°C; however, first melting likely occurred at a lower temperature but was not recognizable owing to the small size of the MI combined with the fact that the MI were filled with crystals that made it difficult to recognize the beginning of melting. At 780°C, all of the crystals in some of the smaller MI had melted to produce MI containing melt ± a vapor bubble. With continued heating, more MI homogenized (all crystals in the MI melted) and the homogenization temperatures generally increase with increasing MI size. This same behavior was observed by Student and Bodnar (1999) during heating studies of synthetic silicate MI.

The volume proportion of the bubble in the incompletely homogenized MI (after all solids had dissolved) was about 0.5-2 vol% and was relatively consistent within a given assemblage, although exceptions were observed. Because most of the completely homogenized MI in this study were generally too small to analyze by EMP, and because larger, completely homogenized MI were rare, MI containing a small vapor bubble were

included in the suite of MI selected for further analyses. As the bubbles are assumed to contain only volatile species (H_2O and CO_2), the presence of the vapor bubble is not expected to affect concentrations of non-volatile components in the melt.

Raman spectroscopy

Both unheated and heated MI were analyzed by Raman spectroscopy at Virginia Tech using a JY Horiba LabRam HR (800 mm) Raman spectrometer. Excitation was provided by a 514 nm Ar^+ laser with an output power of 100 mW at the source. Measurements were collected through a 100 \times objective using a 400 μm confocal hole, and slit width of 150 μm . Gratings, collection times, and spectral region of interest varied depending on the phase being analyzed, as described below. The 600 groove/mm grating were used during analysis of the crystallized solid phases in unheated MI, and three 45s scans with the spectrometer centered at 1100 cm^{-1} were collected and averaged during each analysis.

Raman analysis of the glass phase in reheated (partially to completely homogenized) MI was conducted to determine the H_2O content of the glass (melt) by measuring the area under the broad H_2O peak (Thomas, 2000; Bodnar and Frezzotti, 2020; Severs et al., 2007) (Fig. S1). Three standard glass samples containing 4.6, 5.9, and 8.1 wt% H_2O were also analyzed twice, both before and after analysis of the MI, using identical collection parameters as were used for the MI. The H_2O content of the glass was then calculated using the average area under the H_2O band for each standard combined with their known H_2O contents (see Bodnar and Frezzotti, 2020; their Figure 3). We note that the small size of the MI precluded analysis by conventional SIMS or FTIR to determine the H_2O and CO_2 content of the glass.

Raman analyses of the vapor bubbles in MI were conducted to test for the presence of CO₂ in the bubble in partially-homogenized MI. Some coexisting fluid inclusions were also analyzed by Raman spectroscopy to test for the presence of CO₂. During analysis of the vapor bubble in MI at room temperature, the portion of the spectrum at $\sim 3575\text{ cm}^{-1}$ corresponding to H₂O, was also interrogated. However, the spectrum showed only the broad band that characterizes H₂O dissolved in the glass (Fig. S1b). Previously, Berkesi et al. (2009) and Lamadrid et al. (2014) showed that if H₂O occurs as a thin rim surrounding a CO₂ bubble it can be undetectable during analysis at room temperature, but that if the inclusion is heated to homogenize the H₂O and CO₂ into a single phase the H₂O peak can often be observed. Thus, in order to test further for the presence of H₂O in the vapor bubble, the MI was heated to 300°C, and analysis at this temperature revealed a small shoulder on the broad H₂O band (Fig. S1c). The position of the shoulder on the broad band corresponds to the location of the band for H₂O vapor obtained by analysis of a synthetic FI at 250°C (Fig. S1d) and supports microthermometric data that indicates the presence of liquid H₂O in the bubble at low temperatures (room temperature or lower).

The Raman data were analyzed using LabSpec 5 software to fit the peaks using the Gaussian method. A baseline correction was applied automatically by fitting multiple line segments between local minima in the spectrum. We note that the method selected to fit the water band (Gaussian, Lorentzian, or mixed Gaussian-Lorentzian) has little effect on the relative peak areas determined. The integral function in the software was used to determine the area of the water band in the re-homogenized MI and in standard glasses.

Electron Microprobe (EMP)

Electron microprobe analysis of MI with a high volatile content is challenging. Typically, analyses are conducted with a broadened electron beam and at high accelerating voltage (20 keV) in order to minimize current density, sample heating, and the associated analytical artifacts such as Na migration (Morgan and London, 1996; 2005). However, the small size (2–7 μm) of the MI available for microprobe analyses in this study severely limited our ability to mitigate these effects.

Our approach was to use a field emission scanning electron microscope (FE-SEM) fitted with an energy dispersive spectrometry silicon drift detector (EDS-SDD), rather than a tungsten source electron microprobe (EMP). The small electron beam size (~ 10 nm) and high-resolution imaging ensured that the analytical spot could be well centered within a melt inclusion, and therefore any overlap of the X-ray interaction volume with the host quartz crystal could be minimized. This approach helped to avoid the occurrence of mixed phase analyses but was limiting in other ways (see Results).

EDS. Prior to microanalysis, the grain mount was coated with carbon using a Denton Bench Top Turbo vacuum coater. The samples were then examined and analyzed at the USGS in Reston, VA using a Hitachi SU-5000 Schottky FE-SEM fitted with an EDAX Quantax 30 mm² EDS-SDD. Concurrent observation in backscatter electron and panchromatic cathodoluminescence helped to locate MI that exhibited low BSE contrast with the host quartz. EDS analyses were collected for 50 seconds at an accelerating voltage of 15 keV, 50 spot position (~ 4 nA probe current), and a working distance of 10 mm. Modeling with Casino v. 2.48 (Drouin et al., 2007) indicates that at this accelerating voltage, the depth of the

interaction volume was $\sim 2 \mu\text{m}$. Concentrations were calculated from the count data using the factory standardization and eZAF correction scheme.

WDS. For comparison, following EDS analysis, the MI from quartz crystal Z1, which were all $>4 \mu\text{m}$ in diameter, were also analyzed by wavelength dispersive spectroscopy (WDS). Quantitative EMP analyses of major and minor elements were obtained at the USGS in Reston, VA using a JEOL JXA-8900 five spectrometer, fully automated electron microprobe operating under Probe for EMP software (Donovan et al., 2015). EMP analyses were conducted at an accelerating voltage of 15 keV with a 10 nA probe current, and using a $1 \mu\text{m}$ diameter probe spot. Crystals used for analysis and x-ray lines analyzed were TAP = NaK α , SiK α , MgK α , AlK α ; LIFH = TiK α , BaK α , FeK α , MnK α , PETJ = PK α , SK α , KK α , CaK α , ClK α , and LDE = FK α . On-peak count times were 30 seconds for F and Cl and 10 seconds for all other elements. Off-peak count times were half the on-peak time on either side of the peak of interest. The analyses were corrected for instrumental drift, deadtime, and electron beam/matrix effects using a Phi-Rho-Z algorithm (Armstrong, 1988; Donovan et al., 2015) and the mass absorption coefficients of Henke et al. (1982). Time dependent intensity corrections were applied to the Na and F counts. Standards were appropriate synthetic or natural materials available in the Reston Microbeam Laboratory and were analyzed under the same conditions as the unknowns, but with a spot diameter of $20 \mu\text{m}$. Basaltic and rhyolitic glass standards GLMP and GLRS (Huebner and Woodruff, 1985) and obsidian from SPI Supplies, Inc. were analyzed before and after the analysis of unknowns to test for accuracy. Relative accuracy of these analyses, based upon comparison between measured and published compositions, is $\sim 3 \%$ for element concentrations $>2 \text{ wt}\%$ and $\sim 10\%$ for element

concentrations between 0.1 and 2 wt%. However, unknown analyses are less accurate due to the analytical challenges presented by the small size and high volatile content of the melt inclusions.

Rhyolite-MELTS modeling

The Rhyolite-MELTS simulator (Ghiorso and Gualda, 2015; Gualda et al., 2012) was applied in this study to constrain the evolution (mineral assemblages and melt composition) of the Taishanmiao silicate melt that formed the batholith. The modeling effort was undertaken to test if the composition of the pegmatite melt determined from the EMP analyses of the MI in the pegmatite is consistent with melt compositions predicted by Rhyolite-MELTS during fractional crystallization of the melt that formed the Taishanmiao batholith. The Rhyolite-MELTS simulations used a starting melt composition based on published bulk rock analyses for the batholith (Gao et al., 2014; Jin et al., 2018; Wang et al., 2016; Ye et al., 2008) (Table 1). Simulations were run for a range of H₂O contents ≤ 2 wt%, which is an approximate upper limit for high-temperature, A-type granite or rhyolite that forms at >900 °C (Creaser and White, 1991), and is also consistent with the low abundances of hydrous phases observed. We conducted simulations over a broad range of pressures up to 5 kbar, which was the maximum pressure for formation of the batholith estimated from the bulk rock characteristics by Wang et al. (2016). Jin et al. (2018) reported a lower limit for the oxygen fugacity equal to Nickel-Nickel Oxide (NNO), and we examined various oxygen fugacities from this lower value up to two log units above the QFM (Quartz-Fayalite-Magnetite) oxygen buffer (QFM+2). The liquidus temperature was calculated using Rhyolite-MELTS after establishing initial

conditions (melt composition, pressure and oxygen buffer). Closed-system equilibrium crystallization was assumed, and the model was run beginning at the liquidus and cooling in 5°C temperature increments at constant pressure.

The Taishanmiao batholith is composed of predominantly high-K, calc-alkaline granite, which accounts for ≥ 96 vol% of the igneous batholith. The remainder of the batholith volume is composed of less abundant pegmatites (2-4 vol%) and minor quartz veins (Qi, 2014; Ye et al., 2008). After running a series of test models at various pressures and oxygen fugacities, run conditions of 3.3 kbar and oxygen fugacity of QFM+2 were found to predict mineral phases and their individual proportions after ~ 96 % crystallization that are consistent with field and petrographic observations of the Taishanmiao granite, and are interpreted to reasonably represent the conditions during crystallization of the magma up to the point at which pegmatites begin to form. At higher pressures, for example, pyroxene is predicted to precipitate but this phase has not been reported from the batholith. The predicted liquidus temperature from Rhyolite-MELTS at these conditions was $\sim 1074^\circ\text{C}$. Note that the actual liquidus at this pressure is likely lower than this value. This reflects the fact that Rhyolite-MELTS does not include an appropriate thermodynamic model for biotite, and this results in an under-estimate of the predicted amount of biotite that crystallizes (Gualda et al., 2012; Schiller and Finger, 2019). This difference is likely because the biotite composition in the model $[\text{K}(\text{Fe}_{0.01}\text{Mg}_{0.99})_3\text{AlSi}_3\text{O}_{10}(\text{OH})_2]$ is different than the composition of Taishanmiao biotite $[(\text{K}(\text{Fe}_{0.46-0.59}\text{Mg}_{0.41-0.54})_3\text{AlSi}_3\text{O}_{10}(\text{F}, \text{OH})_2)]$ determined by previous EMPA analyses (Jin et al., 2018), i.e., the biotite composition predicted by the model contains less Fe and more Mg than that measured Taishanmiao biotite. Accordingly, more Fe should substitute for

Mg in the biotite and thereby increase the predicted biotite content in the mineral assemblages at the expense of forming magnetite (1.0 vol%), which is higher in the model predictions compared to the minor magnetite abundance based on petrographic observation. The under-estimate in amount of biotite, in turn, means that less water is consumed during melt crystallization. If the melt contained a higher initial water content, the liquidus temperature would be lower. Nevertheless the predicted liquidus temperature is within the range of liquidus temperatures (815-1077°C) estimated from zircon saturation thermometry (Wang et al., 2016). If none of the zircon is inherited from a precursor protolith, zircon saturation thermometry provides a minimum estimate of the liquidus temperature (Miller et al., 2003; Watson and Harrison, 1983).

After simulating ~96% crystallization of the granitic melt, the mineral assemblage consists of >83 wt% quartz plus K-feldspar, with lesser amounts of plagioclase (~14 wt%) and other minor phases (Table 2), and the temperature is predicted to be ~734°C.

MELT AND FLUID INCLUSION PETROGRAPHY

Doubly-polished sections ~0.08 - 0.12 mm thick were prepared for petrographic and microthermometric analysis of MI and FI. The MI are partly to completely crystallized (Fig. 4b), which is typical of MI in plutonic rocks (Bodnar and Student, 2006), and they commonly occur in 3D or planar groups within quartz crystals that are intergrown with K-feldspar (Fig. 4a). MI typically do not occur along obvious former growth surfaces, nor do they occur along obvious fractures that traverse entire crystals. As such, the MI cannot be definitively classified as either primary or secondary in origin. Most of the inclusion assemblages occur in random

groups within crystals and are of indeterminate (or unknown) temporal origin, using the terminology proposed by Goldstein and Reynolds (1994). We note that the occurrence of randomly distributed inclusions, and inclusions in 3D groupings within crystals, is consistent with a primary origin (Roedder, 1984). Most importantly with respect to this study, the presence of MI in quartz crystals in the pegmatites indicates that the inclusions trapped a silicate melt, and that melt must have been present when the quartz crystals in the pegmatites formed.

The MI are generally spherical to ellipsoidal, with some having an irregular shape, and commonly range from 1 to 30 μm in diameter, with most being between 3 and 15 μm (Fig. 4a, b). MI are distinguished from FI based on the presence of abundant crystals filling most of the MI volume, while FI typically contain only liquid and vapor. The mostly crystallized MI observed in this study usually contain a “bubble” that contains vapor \pm a liquid phase. Here, we refer to these as “vapor bubbles” or “vapor phase”, recognizing that liquid H_2O was detected in some bubbles based on room temperature petrography and/or Raman analysis at elevated temperature. The vapor phase appears to occupy between 5 and 30 vol% of the MI. After heating the MI to homogenize the solids followed by quenching, most MI contained either only glass or glass + vapor (Fig. 5a, b). Some MI are incompletely homogenized and contain large bubbles after heating (Fig. 5c), and these likely trapped various proportions of the coexisting magmatic vapor phase \pm crystals in addition to melt, or have leaked during heating. These inclusions are not considered further here.

Two-phase, liquid + vapor (L+V) FI coexist with crystallized MI in several cases (Fig. 4c). The FI are mostly rounded to elongate in shape and liquid-rich, with the vapor phase

occupying ~20-50 vol% of the inclusion. All FI homogenized to the liquid phase when heated. The FI vary in size from 2 to 20 μm , with a few up to 35 μm in diameter. Raman spectroscopic analysis detected CO_2 in the vapor phase of most fluid inclusions.

Fluid inclusions similar to those observed coexisting with MI (Fig. 4c) are also observed randomly distributed in some quartz crystals (Fig. 4d, e), without any associated MI. These FI are interpreted to have trapped the same fluid that was being trapped along with MI in other parts of the crystal. Some secondary FI along late, healed fractures were also observed (FI in upper left of Fig. 4d) but these were not studied here.

H_2O and CO_2 concentrations of the trapped melt

Several approaches have been used by workers to determine the total volatile content (H_2O and CO_2) of MI. If the MI contains a single glass phase, without a vapor bubble or daughter minerals, one would analyze the glass using FTIR or SIMS to directly determine the H_2O and CO_2 concentrations. If the MI contains a vapor bubble in addition to glass, one can analyze the glass by FTIR or SIMS and analyze the vapor bubble by Raman to determine the CO_2 density and reconstruct the total volatile content based on volume proportions of glass and vapor bubble. If the glass cannot be analyzed, a minimum CO_2 content of the MI can be estimated based on the recognition that in most MI, >50% of the CO_2 is contained in the vapor bubble (Steele-MacInnis et al., 2011; Moore et al., 2015). This technique assumes that the vapor phase is pure CO_2 . Finally, if the MI as found is partially to completely crystallized and contains a vapor bubble, then it is necessary to heat the MI to homogenize the contents before analysis. If, after heating and quenching, the MI contains a homogeneous glass phase, then the

method described above for glass inclusions can be applied. Similarly, if, after quenching, the MI contains a glass phase and a vapor bubble, the MI volatile content can be reconstructed as described above for MI that contain a vapor bubble.

None of the methods described above are applicable to the MI in this study, for several reasons. Most importantly, the small size of the MI precludes analysis of the glass phase by FTIR or conventional SIMS analysis, and the CO₂ content of the glass is too low to be detected and quantified by Raman (Bodnar and Frezzotti, 2020). Additionally, the method of reconstructing the CO₂ content of the glass based on Raman analysis of the vapor bubble to determine the CO₂ density is only valid if the bubble contains essentially pure CO₂, and Raman analyses of the bubble in MI heated to 300°C in this study confirms the presence of an unknown amount of H₂O in the vapor bubble. As such, here we have estimated the H₂O and CO₂ concentrations in the trapped melt based on limited observations and data, combined with reasonable assumptions concerning the behavior of volatiles in melts at crustal *PT* conditions. Raman analysis of reheated MI conducted at room temperature detected H₂O in the glass phase in all inclusions analyzed (Fig. S1), and the Fermi diad of CO₂ was observed during analysis of the vapor phase of those MI that contained a glass phase plus a bubble. Also, the Raman peak corresponding to vapor H₂O was observed in the MI bubble when it was analyzed at 300°C (Fig. S1c). Thus, we know that (1) the melt (glass) contains H₂O, and the concentration of H₂O in some MI was quantified by Raman analysis, and (2) the vapor phase that was in equilibrium with the melt contains both H₂O and CO₂. Based on these two facts, we can also state that the glass (melt) must also contain some amount of CO₂ based on known partitioning behavior of H₂O and CO₂ between melts and coexisting vapor at crustal *PT*

conditions. Using this information, the total H₂O and CO₂ contents of the trapped melt were estimated as described below.

The intensity or area of the Raman band obtained by analysis of the glass in the MI over the range 3000 to 3750 cm⁻¹ is directly proportional to the H₂O concentration in the glass (Thomas, 2000). Accordingly, the ratio of the peak areas obtained from the standard and from the sample (spectra collected using identical collection parameters) is proportional to the ratio of the H₂O content of the standard and the sample (Figs. S2b, S3). The water content of the homogenized MI obtained in this manner ranges from 3.2 - 4.5 wt%, with an average content of 4.1 wt% and a standard deviation of ~0.5 wt% (Table S1; Fig. S3). We note that the calibration standards used during the analyses all have slightly higher water contents compared to the MI. However, owing to the linear relationship between peak area and water concentration over the range from ~0 to 17 wt% H₂O reported by Thomas (2000; his Fig. 3), we are confident that errors associated with the extrapolation to lower water concentrations are minimal. It is possible that the MI could have lost some amount of water after trapping, based on the results of Severs et al. (2007) who documented experimentally that MI in quartz lost up to 75% of their initial water content when held at 800°C and 1 kbar for ~63 days. We also note that electron microprobe (EMP) analyses suggested that some amount of excess quartz was dissolved from the MI walls during heating to homogenize the MI. This, in turn, would dilute the H₂O (and CO₂) concentrations in the glass phase – thus, the H₂O concentrations reported here are considered to represent minimum concentrations for the trapped melt.

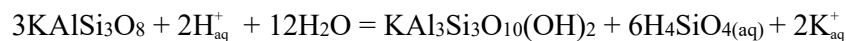
Raman analysis of the glass phase in the MI failed to detect CO₂, which is not surprising

given that Morizet et al. (2013) report a minimum detection limit of ~2,000 ppm for CO₂ using Raman spectroscopy. While we are unaware of any published data on CO₂ contents of MI from environments similar to that studied here, CO₂ contents of rhyolitic to dacitic MI from arc volcanoes reported by Wallace (2005) are generally less than 1,000 ppm. Similarly, Anderson et al. (2000) reported CO₂ contents in rhyolitic MI from the Bishop Tuff that ranged from 19-150 ppm in early erupted MI, to 117-761 ppm in late-erupted MI. Here, we have assumed that the trapped melt contains 500 ppm CO₂ (based on results of the Rhyolite-MELTS modeling) to reconstruct the evolution of the MI during formation of the pegmatites. We note that the actual CO₂ concentration selected for the trapped melt has little effect on the conclusions reached below because we are only considering relative changes in the MI properties during pegmatite formation.

Identification of daughter crystals in the unheated MI

Raman spectra were collected from crystallized phases in 15 unheated MI in quartz crystals A2, A5 and Z1. We note that, owing to the fine-grained and intergrown texture of the crystals in the MI, it was generally not possible to obtain an analysis of a single phase without some contribution to the spectrum from other nearby phases, including the quartz host. As such, eleven analyses of the daughter crystals show similar spectra (Spectrum Type I, Fig. S2a) that are interpreted to represent a mixture of quartz and mica (most likely muscovite). The quartz signal is interpreted to represent contributions from the host quartz. Based on petrographic observations and the Raman spectra, we conclude that the major crystalline phase in the MI is mica. The mica (muscovite) might represent the end product of reaction

between K-feldspar daughter crystals with H₂O that exsolved from the melt during crystallization according to (Helgeson, 1969):



Dissolved silica produced by the reaction would precipitate as quartz on the inclusion walls.

The Raman spectra obtained from four other MI show peaks characteristic of quartz and mica observed in the other eleven MI, plus a complex band in the range 1000 - 800 cm⁻¹ (Spectrum Type II, Fig. S2a). The origin of these bands in the range 1000 - 800 cm⁻¹ is unknown, although it has been reported that bands in the region of 1200 - 800 cm⁻¹ might be caused by silicon-oxygen stretching vibrations of tetrahedral groups in the silicate glass (McMillan et al., 1982; Kucharczyk et al., 2018), suggesting that these MI still contain some glass in addition to crystals. We note that peaks in the region 1000 - 800 cm⁻¹ are not present when the quartz host adjacent to the MI is analyzed, indicating the bands originate within the MI.

Fluid inclusions that coexist with MI in quartz crystals Z2 and A5 were also analyzed with Raman spectroscopy. The results show the presence of CO₂ in the bubble, and only liquid H₂O was detected in the liquid phase when analyzed at room temperature (Fig. S5). The data confirm that the fluid phase in equilibrium with the melt during pegmatite formation contained both H₂O and CO₂.

Fluid inclusion microthermometry

Microthermometric analysis was conducted on six FI coexisting with MI (cf., Fig. 4c) from two assemblages that were also analyzed by Raman spectroscopy. The

microthermometric data for the FI are consistent and are summarized in Table S2. Final ice-melting temperatures ($T_m \text{ ice}$) range between -4.9°C and -5.6°C , and CO_2 clathrate melting temperatures ($T_m \text{ CO}_2\text{-clathrate}$) range from 5.1°C to 6.3°C (Table S2). During heating, all fluid inclusions homogenized to the liquid phase by the disappearance of the vapor bubble, with a narrow range of homogenization temperature (T_h) of 278.4°C to 306.4°C . The salinity of the fluid inclusions estimated by the model of Steele-MacInnis (2018) is 5.0 - 5.7 wt% NaCl equivalent (Table S2). In addition to FI that coexist with MI, homogenization temperatures were also measured for some randomly distributed FI (cf. Fig. 4e), with T_h spanning a relatively wide from 283°C to 370°C . All of the FI studied are interpreted to have been trapped during the formation of the pegmatite and thus their isochores should define the range of PT conditions for pegmatite formation. Isochores for the FI were calculated using the model of Steele-MacInnis (2018).

EDS and WDS results of re-homogenized MI

EDS data were collected on 14 MI from three melt inclusion assemblages contained in 3 different quartz crystals. One MI from crystal A5 yielded an anomalously high SiO_2 content and is interpreted to be compromised by contribution from the host quartz, or alternatively, the elevated SiO_2 content is the result of overheating the MI during homogenization, as described above, and is not considered further. Two MI from crystal A5 yielded high Al_2O_3 and TiO_2 concentrations that are interpreted to reflect mixed analyses that included glass plus incompletely dissolved muscovite, as was clearly observed in 1 of the 2 MI analyzed (Fig. S4) and are not considered further. Results for the remaining 11 analyses are presented in Table S3

along with 3 replicate analyses of MI from crystal Z1 collected by WDS methods.

In general, the WDS and EDS data from crystal Z1 show good agreement for all elements except potassium. The K_2O concentrations determined by WDS are significantly lower than that determined by EDS. There is no obvious explanation for the disagreement. The Na_2O and Al_2O_3 concentrations are also slightly lower in the WDS analyses. However, this difference was expected and can be explained, in part, by sodium migration during analysis (Morgan and London, 2005). Indeed, a decrease in sodium count rate was observed and corrected for during EMP analysis. This suggests that the determined Na_2O concentrations from EDS and WDS analyses should be viewed as lower limits.

Analyses of MI within individual crystals (i.e. three MI assemblages) are relatively consistent, but each crystal yields a unique composition. Considering only the EDS data, the major compositional variations are associated with K, Na, Al, and F. Variations in the concentrations of these elements in MI likely reflects trapping of MI at different stages in the crystallization history of the pegmatites. As described below, the proportions of crystals and melt in the pegmatite volume may have varied significantly during pegmatite formation, and may have shown reversals whereby an episode of crystal growth was followed by an episode of crystal resorption into the melt. Thus, MI from different assemblages (i.e. from three crystals examined here) with variable compositions likely represent MI entrapment at different stages during magma evolution. The range in Al_2O_3 content from 11.5 - 14.9 wt% likely reflects different proportions of K-feldspar and quartz crystallization (the main minerals in the Taishanmiao pegmatite). Sodium and potassium are generally considered to be the two major cations in the exsolved magmatic fluid phase, and fluid exsolution should therefore lead to

modification of their concentrations in the melt. F commonly behaves incompatibly during crystallization of quartz and alkali-feldspar and remains in the granitic melt during aqueous fluid phase exsolution (see details in Discussion section). F is thereby enriched in the pegmatite melt during the evolution process and is likely responsible for the wide variation in F content in MI that ranges from 0.3 - 1.4 wt%.

The H₂O content of the MI cannot be estimated from the EDS analyses because the factory standardization was used and measured oxide results must sum to 100%. The WDS analyses of crystal Z1, however, suggest an H₂O content of 2.8 - 3.7 wt%, lending support to the H₂O contents of 3.2 - 4.5 wt% determined from Raman analysis (Table S1).

Results of Rhyolite-MELTS simulation

The Rhyolite-MELTS simulations used the starting composition listed in Table 1. We estimated the initial volatile content of the melt (0.26 wt% H₂O and 22 ppm CO₂) iteratively based on the degree of crystallization required to produce the composition of the MI. We also assumed a constant pressure of 3.3 kbar during crystallization, with oxygen fugacity buffered at QFM+2. From the initiation of crystallization (0%) up to ~96 wt% crystallization, the model predicts crystallization of quartz, K-feldspar, plagioclase, biotite, and spinel (classified as magnetite here from the simulated mineral chemical result) (Fig. 6). The predicted mineral assemblage is consistent with petrographically-determined mineral assemblages of the Taishanmiao granite, which occupies ≥ 96 vol% of the Taishanmiao batholith. Also, the proportions of individual phases obtained from thermodynamic modeling are consistent with petrographic observations. Specifically, after 96 wt% crystallization at ~734°C, representing

the beginning of the pegmatite-forming stage, the melt-free normalized mineral assemblage consists of 51.1 vol% K-feldspar, 33.6 vol% quartz, 14.1 vol% plagioclase, 0.1 vol% biotite, and 1.0 vol% magnetite (Table 2). The mineral proportions predicted by the Rhyolite-MELTS model are consistent with field and petrographic observations of the Taishanmiao granite reported by Jin et al. (2018) and Wang et al. (2016), with the exception of biotite (0.1 vol% predicted compared to 1-5 vol% biotite reported from field and petrographic observations) and magnetite. However, it is known that Rhyolite-MELTS (Gualda et al., 2012) underestimates the biotite content in other settings (Schiller and Finger, 2019) and the small difference does not affect the model developed here for formation of the pegmatites. After ~96% crystallization, representing the beginning of the pegmatite stage, the melt contains 6.3 wt% H₂O and 500 ppm CO₂ and is volatile-undersaturated.

PVTX evolution of pegmatite during crystallization

The PVTX evolution during pegmatite formation was calculated assuming constant mass and volume conditions. The residual melt remaining after 96% of the Taishanmiao granite was assumed to represent the starting melt composition. As such, the melt was generally rhyolitic in composition and contained 6.3 wt% H₂O and 500 ppm CO₂ and was volatile undersaturated. At each temperature, the first step was to calculate a degassing path for the melt using the VolatileCalc simulator and assuming closed-system behavior (Newman and Lowenstern, 2002). Thus, at 734°C, a rhyolite melt containing 6.3 wt% H₂O and 500 pm CO₂ becomes volatile saturated at 2,653 bars, and the volatile phase in equilibrium with the melt at these

conditions contains 79.6 mol% H₂O and 20.4 mol% CO₂. The density of the vapor phase at 734°C and 2,653 bars is 0.618 g/cm³ (Connolly and Bodnar, 1983).

At each temperature along the cooling path, starting at the pressure at which the melt becomes saturated in volatiles, the pressure was decreased incrementally. At each new pressure, the solubilities of H₂O and 500 pm CO₂ in the melt were calculated, as well as the composition and density of the vapor phase in equilibrium with the melt at the new pressure. Then, the melt was incrementally crystallized, and at each increment of crystallization the volume change associated with crystallization was calculated based on the known volume of fusion from Lange and Carmichael (1990). Accordingly, the mineral-averaged volume of fusion for the pegmatite melt is 5.6 cm³/mol of melt crystallized. The volume change associated with crystallization represents the volume available to host the vapor phase that is in equilibrium with the melt. At each increment of crystallization, the volatile components were distributed between the melt and the fluid phase according to the partitioning behavior predicted by VolatileCalc, and the volumes of the melt, crystals and vapor phase were calculated based on known densities and amounts of the various phases. At each increment, the sum of the masses and volumes of the phases was compared to the total masses of the components in the melt and the volume of melt after 96% of the granite had crystallized. If the calculated masses or volumes differed by more than 0.1% from the original mass and volume of the trapped melt, mass and volume balance were not possible at that temperature and pressure for that amount of crystallization. Then, the proportion of

the melt that crystallized was incrementally increased and the process was repeated.

As an example, at 700°C and 2,400 bars, the melt will contain 6.09 wt% H₂O and 430 ppm CO₂. The vapor phase in equilibrium with the melt at these conditions contains 82.1 mol% H₂O and 17.9 mol% CO₂ (Newman and Lowenstern, 2002) and has a density of 0.612 g/cm³ (Connolly and Bodnar, 1983). At this PT condition, mass and volume balance are achieved when the cavity contains 38.8 vol% melt, 37.1 vol% crystals, and 24.1 vol% vapor. If, mass and volume balance could not be satisfied for any extent of crystallization between 0-100% at the temperature and pressure of the calculation, it was assumed that it was not possible for those PT conditions to exist in the pegmatite during its formation.

After completing the calculation procedure described above at the temperature of interest and at a pressure along the degassing path predicted by VolatileCalc, the pressure was decreased further and the process was repeated. Thus, at each temperature examined (734°, 700°, 675°, 650° and 625°C), the range of possible pressures in the pegmatite was determined. Accordingly, during isothermal evolution of the pegmatite at 734°C, mass and volume balance are first achieved at a pressure of 2320 bars (Table S4). At this condition, the melt contains 5.92 wt% H₂O and 380 ppm CO₂. Crystallization drives the system to *increasing* pressure, and the system still contains 23.6 volume percent melt, along with 32.5 volume % vapor and 43.9 volume % crystals at 4836 bars, which is the highest pressure tested. The volume percent crystals increases from 0 % at 2320 bars to 43.9

volume % at 4836 bars.

During isothermal evolution of the pegmatite at 700°C, mass and volume balance are first achieved at a pressure of 2254 bars (Table S4). At this condition, the melt contains 5.92 wt% H₂O and 380 ppm CO₂. Similar to the behavior at 734°C, crystallization drives the system to *increasing* pressure, and the system is completely crystallized at the 2651 bars. The volume percent crystals increases from 0 % at 2320 bars to ~60 volume % at 2651 bars, and the cavity contains 37.5 volume percent vapor at the end of crystallization.

At 675°C, mass and volume balance are only achieved within a very narrow pressure window from 2225 to 2255 bars (Table S4). At pressures above 2255 bars, as the volume percent vapor is increased incrementally to determine the volume percent that satisfies mass and volume balance, the entire mass of melt is consumed to form crystals before an equilibrium vapor bubble volume is found and volume balance cannot be achieved. At pressures below 2225 bars, the volume percent vapor required to achieve mass balance does not allow volume balance to be achieved. Thus, within the narrow pressure range from 2225 to 2255 bars, the system evolves from one in which crystals are absent to one containing ~61 volume % crystals instantly, regardless of whether this pressure range is approached from higher or lower pressure conditions.

At 650°C, mass and volume balance are achieved in the pressure range 1958 to 2187 bars (Table S4). However, unlike the evolution of the system at 734°C and 700°C, crystallization begins at the high pressure end of this range and the pressure

in the system *decreases* as crystallization proceeds. Thus, crystallization starts at 650°C and 2187 bars, and the melt contains 5.935 wt% H₂O and 385 ppm CO₂. Crystallization ends when the pressure decreases to 1958 bars, at which point the melt contains 5.643 wt% H₂O and 315 ppm CO₂, and crystals occupy 61 volume % of the original volume.

The evolution of the system at 625°C is similar to that observed at 650°C. Thus, mass and volume balance are achieved in the pressure range 2155 to 1737 bars and pressure *decreases* as crystallization proceeds (Table S4). At the end of crystallization the pegmatite contains 61 volume percent crystals and ~39 volume percent vapor.

If this simple mass and volume balance model can be applied to predict the *PVTX* evolution of a miarolitic class, segregation-type pegmatite that undergoes crystallization under closed system, isochoric conditions, the results suggest that pressure within the pegmatite will fluctuate as the pegmatite cools, rather than following a monotonic path with pressure continuously decreasing. We invoke this process to explain the development of the pegmatitic texture (i.e., large crystals). The pressure fluctuations result in liquidus deficits of varying magnitude within the pegmatite, leading to alternating periods of mineral growth and dissolution, serving to coarsen the crystals and reduce surface area and surface free energy, in a manner similar to Ostwald ripening.

REFERENCES CITED

- Anderson, A.T., Davis, A.M., Lu, F. (2000) Evolution of Bishop Tuff rhyolitic magma based on melt and magnetite inclusions and zoned phenocrysts. *Journal of Petrology*, 41, 4449-4473.
- Armstrong, J.T. (1988) Quantitative analysis of silicate and oxide minerals: Comparison of Monte Carlo, ZAF and Phi-Rho-Z procedures. In D.E. Newbury (Ed.), *Microbeam analysis*, p. 239-246. San Francisco Press, California.
- Berkesi, M., Hidas, K., Guzmics, T., Dubessy, J., Bodnar, R.J., Szabó, C., Vajna, B., Tsunogae, T. (2009) Detection of small amounts of H₂O in CO₂-rich fluid inclusions using Raman spectroscopy. *Journal of Raman Spectroscopy*, 40, 1461-1463.
- Bodnar, R.J., Frezzotti, M.L. (2020) Microscale chemistry: Raman analysis of fluid and melt inclusions. *Elements*, 16, 201-205.
- Bodnar, R.J., Student, J.J., (2006) Melt inclusions in plutonic rocks: petrography and microthermometry. In: Webster, J.D. (Ed.), *Melt Inclusions in Plutonic Rocks*, p. 1–25. Mineralogical Association of Canada, Montreal, Québec, Canada.
- Connolly, J.A.D., Bodnar, R.J. (1983) A modified Redlich-Kwong equation of state for H₂O-CO₂ mixtures: Application to fluid inclusion studies. *EOS*, 64, 350.
- Creaser, R.A., White, A.J. (1991) Yardea Dacite—large-volume, high-temperature felsic volcanism from the Middle Proterozoic of South Australia. *Geology*, 19, 48-51.
- Donovan, J., Kremser, D., Fournelle, J., Goemann, K. (2015) Probe for EPMA: Acquisition, automation and analysis, version 11: Eugene, Oregon, Probe Software. Inc., <http://www.probesoftware.com>.
- Drouin, D., Couture, A.R., Joly, D., Tastet, X., Aimez, V., Gauvin, R. (2007) CASINO V2. 42—a fast and easy-to-use modeling tool for scanning electron microscopy and microanalysis users. *Scanning: The Journal of Scanning Microscopies*, 29, 92-101.
- Esposito, R., Klebesz, R., Bartoli, O., Klyukin, Y., Moncada, D., Doherty, A., Bodnar, R.J. (2012) Application of the Linkam TS1400XY heating stage to melt inclusion studies. *Open Geosciences*, 4, 208-218.
- Gao, X.Y., Zhao, T.P., Bao, Z.W., Yang, A.Y. (2014) Petrogenesis of the early Cretaceous intermediate and felsic intrusions at the southern margin of the North China Craton: Implications for crust–mantle interaction. *Lithos*, 206-207, 65-78.
- Ghiorso, M.S., Gualda, G.A.R. (2015) An H₂O–CO₂ mixed fluid saturation model compatible with rhyolite-MELTS. *Contributions to Mineralogy and Petrology*, 169, 1-30.
- Gualda, G.A.R., Ghiorso, M.S., Lemons, R.V., Carley, T.L. (2012) Rhyolite-MELTS: a Modified Calibration of MELTS Optimized for Silica-rich, Fluid-bearing Magmatic Systems. *Journal of Petrology*, 53, 875-890.
- Goldstein, R.H., Reynolds, T.J. (1994) Systematics of fluid inclusions in diagenetic minerals: SEPM Short Course, 31, 199.

- Helgeson, H.C. (1969) Thermodynamics of hydrothermal systems at elevated temperatures and pressures. *American Journal of Science*, 267, 729-804.
- Henke, B. L., Lee, P., Tanaka, T. J., Shimabukuro, R. L., Fujikawa, B. K. (1982) Low-energy X-ray interaction coefficients: Photoabsorption, scattering, and reflection: E= 100–2000 eV Z= 1–94. *Atomic data and nuclear data tables*, 27, 1-144.
- Huebner, J., Woodruff, M.E. (1985) Chemical compositions and critical evaluation of microprobe standards available in the Reston microprobe facility. 2331-1258, US Geological Survey.
- Jin, C., Gao, X.Y., Chen, W.T., Zhao, T.P. (2018) Magmatic-hydrothermal evolution of the Donggou porphyry Mo deposit at the southern margin of the North China Craton: Evidence from chemistry of biotite. *Ore Geology Reviews*, 92, 84-96.
- Kucharczyk, S., Sitarz, M., Zajac, M., Deja, J. (2018) The effect of CaO/SiO₂ molar ratio of CaO-Al₂O₃-SiO₂ glasses on their structure and reactivity in alkali activated system. *Spectrochimica Acta Part A: Molecular and Biomolecular Spectroscopy*, 194, 163-171.
- Lamadrid, H., Lamb, W., Santosh, M., Bodnar, R.J. (2014) Raman spectroscopic characterization of H₂O in CO₂-rich fluid inclusions in granulite facies metamorphic rocks. *Gondwana Research*, 26, 301-310.
- McMillan, P., Piriou, B., Navrotsky, A. (1982) A Raman spectroscopic study of glasses along the joins silica-calcium aluminate, silica-sodium aluminate, and silica-potassium aluminate. *Geochimica et Cosmochimica Acta*, 46, 2021-2037.
- Miller, C.F., McDowell, S.M., Mapes, R.W. (2003) Hot and cold granites? Implications of zircon saturation temperatures and preservation of inheritance. *Geology*, 31, 529-532.
- Moore, L.R., Gazel, E., Tuohy, R., Lloyd, A.S., Esposito, R., Steele-MacInnis, M., Hauri, E.H., Wallace, P.J., Plank, T., Bodnar, R.J. (2015) Bubbles matter: An assessment of the contribution of vapor bubbles to melt inclusion volatile budgets. *American Mineralogist*, 100, 806-823.
- Morgan, G.B., London, D. (1996) Optimizing the electron microprobe analysis of hydrous alkali aluminosilicate glasses. *American Mineralogist*, 81, 1176-1185.
- Morgan, G.B., London, D. (2005) Effect of current density on the electron microprobe analysis of alkali aluminosilicate glasses. *American Mineralogist*, 90, 1131-1138.
- Morizet, Y., Brooker, R.A., Iacono-Marziano, G., Kjarsgaard, B.A. (2013) Quantification of dissolved CO₂ in silicate glasses using micro-Raman spectroscopy. *American Mineralogist*, 98, 1788-1802.
- Newman, S., Lowenstern, J.B. (2002) VolatileCalc: a silicate melt–H₂O–CO₂ solution model written in Visual Basic for excel. *Computers & Geosciences*, 28, 597-604.
- Qi, Y. (2014) Petrogenesis of Laojunshan and Taishanmiao Granite Plutons in Eastern Qinling, central China. 50 p. M. Sc. Thesis, University of Science and Technology of China, Hefei (in Chinese with English abstract).
- Roedder, E. (1984) Fluid Inclusions, vol. 12. *Reviews in Mineralogy*, Mineralogical

Society of America, Chantilly, Virginia.

- Schiller, D., Finger, F. (2019) Application of Ti-in-zircon thermometry to granite studies: problems and possible solutions. *Contributions to Mineralogy and Petrology*, 174, 51.
- Severs, M.J., Azbej, T., Thomas, J.B., Mandeville, C.W., Bodnar, R.J. (2007) Experimental determination of H₂O loss from melt inclusions during laboratory heating: Evidence from Raman spectroscopy. *Chemical Geology*, 237, 358-371.
- Steele-MacInnis, M. (2018) Fluid inclusions in the system H₂O-NaCl-CO₂: An algorithm to determine composition, density and isochore. *Chemical Geology*, 498, 31-44.
- Steele-MacInnis, M., Esposito, R., Bodnar, R.J. (2011) Thermodynamic Model for the Effect of Post-entrapment Crystallization on the H₂O-CO₂ Systematics of Vapor-saturated, Silicate Melt Inclusions. *Journal of Petrology*, 52, 2461-2482.
- Sterner, S.M., Bodnar, R.J. (1984) Synthetic fluid inclusions in natural quartz I. Compositional types synthesized and applications to experimental geochemistry. *Geochimica et Cosmochimica Acta*, 48, 2659-2668.
- Student, J.J., Bodnar, R.J. (1999) Synthetic fluid inclusions XIV: coexisting silicate melt and aqueous fluid inclusions in the haplogranite-H₂O-NaCl-KCl system. *Journal of Petrology*, 40, 1509-1525.
- Thomas, R. (2000) Determination of water contents of granite melt inclusions by confocal laser Raman microprobe spectroscopy. *American Mineralogist*, 85, 868-872.
- Wallace, P.J. (2005) Volatiles in subduction zone magmas: Concentrations and fluxes based on melt inclusion and volcanic gas data. *Journal of Volcanology and Geothermal Research*, 140, 217-240.
- Wang, C., Chen, L., Bagas, L., Lu, Y., He, X., Lai, X. (2016) Characterization and origin of the Taishanmiao aluminous A-type granites: implications for Early Cretaceous lithospheric thinning at the southern margin of the North China Craton. *International Journal of Earth Sciences*, 105, 1563-1589.
- Watson, E.B., Harrison, T.M. (1983) Zircon saturation revisited: temperature and composition effects in a variety of crustal magma types. *Earth and Planetary Science Letters*, 64, 295-304.
- Ye, H., Mao, J., Xu, L., Gao, J., Xie, G., Li, X., He, C. (2008) SHRIMP zircon U-Pb dating and geochemistry of the Taishanmiao aluminous A-type granite in western Henan Province. *Geological Review*, 54, 699-711 (in Chinese with English abstract).